European Journal of Chemistry 2 (1) (2011) 8-13

European Journal of Chemistry

Journal homepage: www.eurjchem.com

Study on the annealing-dependent photoluminescence properties of SnO_2 cluster-system structures

Yunqing Zhu, Yiqing Chen* and Xinhua Zhang

School of Materials Science and Engineering, Hefei University of Technology, Hefei, Anhui, CN-230009, China

**Corresponding author at: School of Materials Science and Engineering, Hefei University of Technology, Hefei, Anhui, CN-230009, China. Tel.: +86.551.2901365; fax: +86.551.2901362. E-mail address: chenyq63@126.com (Y. Chen).*

ARTICLE INFORMATION

Received: 30 May 2010
Accepted: 11 October 2010
Online: 31 March 2011

KEYWORDS

SnO_2 cluster-system
Thermal evaporation
Photoluminescence
Oxygen vacancy
Bound H_2O molecule
Energy minimization computation

ABSTRACT

SnO_2 cluster-system structures were synthesized via a two-step temperature-rising thermal evaporation method with short oxidation time. Field emission scanning electron microscopy, X-ray diffraction and transmission electron microscopy were used to characterize the morphological and structural feature of the product as nanowire cluster and nanoparticle cluster. The photoluminescence spectra exhibit that, as annealing time in air increases, the intensity of the newly found strong ultra-violet emission decreases while the green emission is increased. Raman spectrum and X-ray photoelectron spectroscopy investigations reveal that the relatively decreasing intensity was dominated by the increasing oxygen vacancy. Further calculation based on the SnO_2 crystal lattices with H_2O molecules at different steps in evaporation process was performed. The result of this calculation confirms that, rather than the influence of H_2O molecules from air, the decreasing intensity is the result of the combined action of the formation of oxygen vacancy and the energetic oxygen compensation in annealing treatment.

1. Introduction

SnO_2 nanostructures has attracted attention of many researchers in the last decade for its wide band gap (E_g = 3.6 eV, at 300 K), low resistivity (10^{-4}–10^6 Ω.cm) and high optical transparency in the visible range (up to 97%). Having these properties, SnO_2 nanostructures can be used in various constructions of chemical sensors [1-3], field-emission transistors [4,5], dye-based solar cells [6], optoelectronic devices etc. [7]. Most of such nanostructures are one dimensional (1-D) and so they can be used as interconnectors in nanodevices and in other promising applications such as in photoluminescence (PL) and electron emitters [8,9]. Although Tang *et al*. have recently grown nickel nanocluster on ZnO nanorod template heterogeneously, [10] so far no SnO_2 nanoparticle cluster has been reported to be homogeneously assembled on 1-D SnO_2 nanowire cluster. In terms of optical property, before putting into practical use, well understanding of the energy band structure of SnO_2 nanostructures is significantly important so as to achieve an explicit comprehension of the origin of the phonon emission which various reporters have ascribed to the oxygen vacancy on the surface [9,11-13]. The levels of the oxygen vacancy have been calculated [14] to successfully predict the position of PL peaks which correspond to some already reported emissions [15-17]. In recent years, however, some researchers discover only a single strong visible emission peaks of about 475-630 nm wavelength from 1-D nanostructure synthesized by using long oxidation time (≥1 hour) [9,18,19]. The effect of annealing treatment on the relative intensity of PL has therefore not been investigated.

Here we report SnO_2 cluster-system structures that were synthesized via a two-step temperature-rising thermal evaporation method with only 25 minutes oxidation time. The annealing-dependent PL properties of SnO_2 cluster-system structures were systematically investigated.

2. Experimental

2.1. Synthesis and annealing treatment

The synthesis was carried out in a horizontal alumina tube furnace. Mixed SnO and graphite powder was used as the raw material and placed in a ceramic boat which was set at the center of the alumina tube. A Si substrate was positioned downstream of the gas flow with a distance of 25 cm from the boat to collect the product. Argon gas, with a flow rate of 35 standard cubic centimeters per minute (sccm), was introduced into the alumina tube to evacuate air. As two-step temperature-rising process, first, the temperature at the center of tube was increased to 1000 °C and was maintained for 20 min. Secondly, the temperature was increased to 1300 °C and Ar +10% O_2 were introduced at 45 sccm for 25 min. The synthesis temperature at the substrate is estimated about 800 °C for our heating system. After the furnace was cooled down to room temperature, a layer of white product was found on the surface of the Si substrate. The annealing treatment was performed at the center of the alumina tube at 700 °C. Air was let into the chamber and the pressure was controlled at about 10^{-3} Torr.

2.2. Instrumentation

A field emission scanning electron microscopy (FESEM, JEOL-JSM-6700F) equipped with an energy dispersive spectroscopy (EDS, Link ISIS, Oxford) was used to observe the morphology of the as-prepared product. The crystal structure

ISSN 2153-2249 (Print) / ISSN 2153-2257 (Online) © 2011 EURJCHEM
DOI:10.5155/eurjchem.2.1.8-13.134

of the product was detected by X-ray diffraction (XRD, D/MaxrB) with Cu-K_α (λ = 1.54 Å) radiation and transmission electron microscopy (TEM, HITACHI H-800). X-ray photo-electron spectroscopy (XPS) and Raman spectra are obtained from XPS spectrometer (ESCALAB 250, Thermo-VG Scientific) and Laser Confocal Raman Microscope (LABRAM-RH, JY. Co., France), respectively. Photoluminescence spectrum of the product was obtained on a fluorescence spectrophotometer (HITACHI F-4500) using a Xe lamp with an excitation wavelength of 325 nm at room temperature.

3. Results and discussion

3.1. Morphology and structure

Figure 1a displays the FESEM images of the grown product. The structures are individually laying on the substrate and composed of two parts: nanowire cluster and nanoparticle cluster which can be seen in Figure 1b. The average diameters of the nanowires and the nanoparticles are estimated to about 70 nm and 120 nm showed in Figure 1c and 1d, respectively. The insets in Figure 1c and 1d are the EDS spectra taken from the corresponding parts. Only Sn and O are observed, which indicates the high purity of the cluster-system of Sn and O.

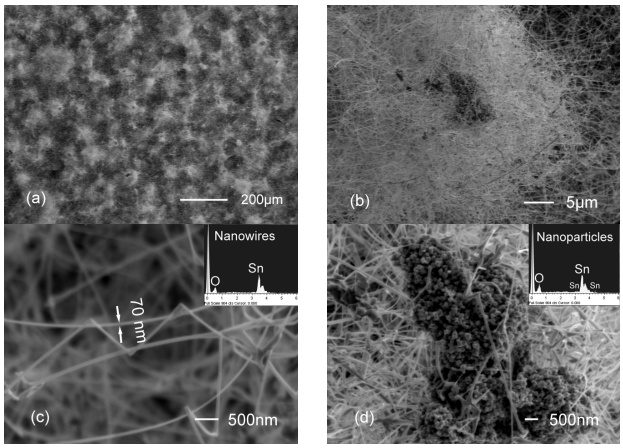

Figure 1. FESEM images of the grown product. (a) Overall view, (b) an individual cluster-system structure, (c) the nanowire cluster part, (e) the nanoparticle cluster part. The insets are EDS spectra obtained from corresponding parts.

Figure 2a is the XRD pattern of the product. All of the peaks prove that the nanostructure is tetragonal rutile structure stannic oxide with lattice constants of a = 4.738 Å and c = 3.188 Å, according to the standard values of bulk SnO_2 (JCPDS 21-1250). No other phases are detected. Figure 2b shows the selected area electron diffraction (SAED) pattern of the typical nanowire with a [10-1] growth direction.

3.2. PL properties

The first principle calculation by Prades *et al.* [14] provides a better understanding of the origin of PL. Figure 3 presents the illustration of the energy band structure based on the calculation which agrees well with the PL spectrum of the product before annealing in Figure 4a where there is a newly found strong ultra-violet emission band at 380 nm (3.27 eV) below the shallow band. Due to a different response time selected in PL measurement for product after annealing, the ultra-violet emission peak has about 17 nm negative shift. Although authors have observed the existence of shallow donor levels contributed by ionized oxygen vacancy (V_O) from ~0.15 up to ~0.30 eV (17 nm width) below the bottom of conduction band (BCB) in electron spin resonance measurements, [20] the continuity of this shallow band is still not clear. A slight blue shift of 0.03 eV was detected after 60 min annealing, which indicates that there are levels of 3.4 eV (annealed 30 min) and 3.43 eV (annealed 60 min) in the shallow band. A peak splitting at 550 nm (2.26 eV) with a total width of 14 nm (from 544 nm to 558 nm) is also generated.

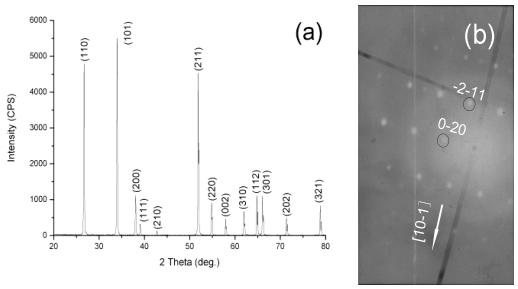

Figure 2. (a) XRD pattern of as-grown product, (b) SAED pattern of the typical nanowire.

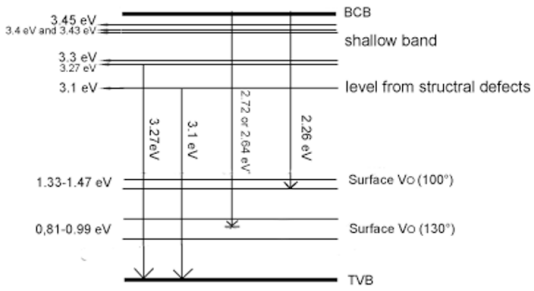

Figure 3. An illustration of the electron energy band structure of tetragonal SnO_2.

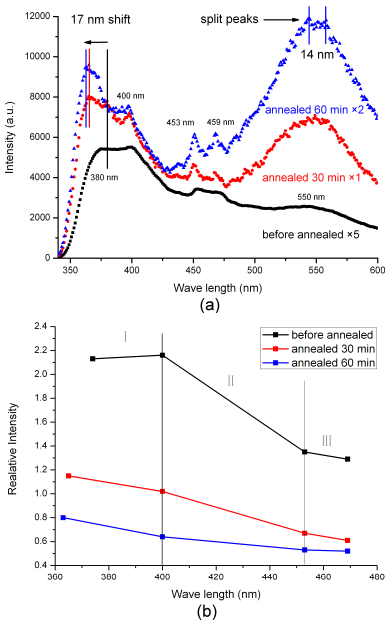

Figure 4. (a) The PL spectra before and after annealing. (b) The evolution of relative intensity of emissions with annealing time. The intensity of 550 nm emission is defined as one unit.

Annealing in air was carried out to investigate the influence of V_O on the PL. Figure 4b exhibits that even 30 min annealing time rather than several hours at higher annealing temperatures (800 °C or higher) on other reports [19,21], the

relative intensities decrease compared to the enhancement of the green emission peak and so it is after a further 30 min annealing (60 min in total). The tendency to the lower values indicates the increasing of V_O. In a given crystal with ionized Vo donor, the possibility of an electron occupying a donor level can be written as equation (1): [22]

$$f_D(E) = \frac{1}{1 + \frac{1}{2}\exp\left(\frac{E_D - E_F}{k_0 T}\right)} \quad (1)$$

where E_D is the energy of V_O donor level, k_0 is Boltzman constant. The Fermi level (E_F) describes the electron distribution in the energy band. Considering the ionization equilibrium, the E_F is incorporated into the following equation:

$$N_c \exp\left(-\frac{E_c - E_F}{k_0 T}\right) = N_v \exp\left(-\frac{E_F - E_v}{k_0 T}\right) + \frac{N_D}{1 + 2\exp\left(-\frac{E_D - E_F}{k_0 T}\right)} \quad (2)$$

where E_c and E_v are the energy values at BCB and the top of valance band (TVB), respectively, and N_c, N_v and N_D are the effective density of BDB, TVB and V_O donor, respectively. Analytic solution of E_F in equation (2) is difficult to work out. The approximate result is $\sim \ln\left(\frac{N_D}{kN_c}\right)$, where k is a coefficient according to the different extinction temperature. The more the effective concentration of ionized oxygen vacancy N_D, the higher the level E_F will shift, which leads to the occupation of more additional electrons above the BCB when they are excited and their direct transition to the V_O level (Sn-coordination angle 100°). The broad emission peak at 550 nm accordingly becomes relatively higher than other emissions with increasing of V_O.

According to the quantum transition theory, the possibility of transition to a given final state can be expressed as equation (3):

$$W_{k\to m} = \left|\frac{1}{i\hbar}\int_0^t H'_{mk} e^{i\omega_{mk}t} dt\right|^2 \quad (3)$$

(k = initial state, m = TVB), where H'_{mk} and ω_{mk} stand for the Hamilton matrix element and transition frequency, respectively. The result of the integrity is as equation (4):

$$W_{k\to m} = \frac{2\pi t}{\hbar} |H'_{mk}|^2 \delta(\varepsilon_m - \varepsilon_k) \quad (4)$$

where $\delta(\varepsilon_m - \varepsilon_k)$ is delta function which only determines the position of the function value. Considering the same time t used in the PL measurement for product after annealing, electrons occupying the higher level will get a higher transition possibility for large $|H'_{mk}|^2$ value. When E_F approaches the shallow band as V_O increases, more electrons in shallow band of a larger $|H'_{mk}|^2$ value has a higher transition possibility to contribute to the ultra-violet emission, which results in the slight blue shift after 60 min annealing. As the E_F level ascends, newly added electrons on higher level than BCB is enough for some electrons to transit to V_O level (544 nm) while others transit to V_O (Sn-coordination angle 100°) level from (100) plane (558 nm) [14], which induces the peak splitting and a further enhancement of green emission. Because of the inadequate electrons remained to have possibility for other transitions, other peak splits or blue shifts are prohibited. The 400 nm emission relates to the structural defects in nanocrystaline particles instead of the concentration of oxygen vacancy [11,23]. As is shown in Figure 4b, an extra contribution to the decreasing of relative intensity at 400 nm due to diminishment of structural defects after annealing leads to a greater change of the slope in region I and II than that in region III.

3.3. Raman spectrum and XPS spectrum study

The tendency to the low relative intensity in Figure 4b concerning the V_O concentration is further studied by Raman spectrum and XPS spectrum. Regardless of the annealing time, the vibrant peak in rectangle within 540-545 cm^{-1} in Figure 5 is identified as S_2 mode to be in line with the defect-induced phonon mode due to the surface disorder and large amount of oxygen vacancies of SnO_2 nanowires [19,29]. Figure 6 are XPS spectra of the product. The O1 peak corresponds to the oxygen ions in SnO_2 lattice of rutile structure and the O2 peak at the range of 531–532 eV is attributed to loosely bound oxygen on the surface [30-32]. No peak at 533 eV from free water is observed [31,32]. All the peaks on XPS spectra have first a positive and then a little negative chemical shift when the product annealed 30 min and 60 min in air, respectively. The ratio O1/Sn in Table 1 is expected to increase during the annealing process in air for the compensation of donor-like oxygen vacancy by energetic oxygen atoms. However, the XPS measurement result gives a contrary result for product annealed 30 minutes, which indicates the increasing of V_O as theoretical reckoning above.

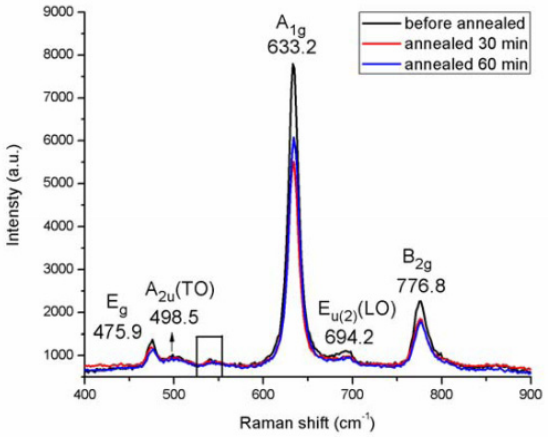

Figure 5. Raman spectra of product before annealed and after annealed 30 min and 60 min in air. The labeled vibration modes are interpreted by various literatures [24-28].

Table 1. XPS results for product before and after annealed in air. The areas of XPS peaks have been adjusted by the sensitivity factors, 0.66 for O and 4.3 for Sn.

	Before annealed	30 min	60 min
O1/Sn	1.49	1.25	1.29
O2/Sn	0.86	1.45	1.15

It is well established that water adsorption on SnO_2 results in the formation of OH surface species [31,32]. Considering the exposure of product in air before and during annealing process, the origin of O2 peak is explained as to be arising from such OH surface species [32,33] provided by coordinated water existing in the SnO_2 lattice shown in Figure 8c. The altering content of coordinated water and lattice water could be the key to the slight changes in O1/Sn and O2/Sn ratios, so that would affect the concentration of V_O and further the PL property. Because of the influence of lattice potential and the perturbation of the relative content of the two kinds of bound water *i.e.* coordinated water (c H_2O) and lattice water (l H_2O), the binding energy of Sn3d and O1s can be slightly changed. Further investigation was carried out by the energy minimization computation.

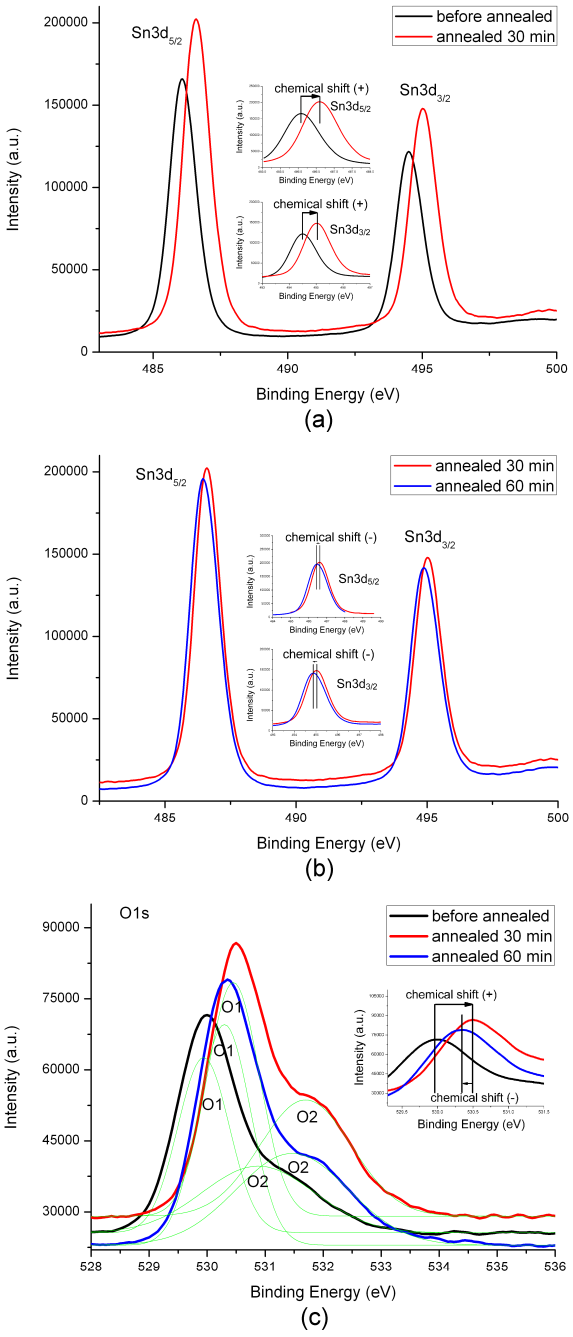

Figure 6. (a) and (b) are XPS spectra of Sn, (c) is XPS spectra of O. The insets in these figures display the chemical shift. The same tendency of chemical shift of O2 peak is not manifested.

3.4. Energy minimization computation

The lattice of 2×3×4=24 units with bound H_2O molecules at different steps in evaporation process under annealing was established to simulate the SnO_2 nanowire. The influence of the deep part of the lattice is considered small enough to be omitted. Figure 7a-h shows the results of simulation and resulting data are listed in Table 2 and 3. According to the charge potential model, the valance electrons E_B of an atom is expressed as follows:

$$E_B = E_B^0 + kq_i + \left(\sum_{j \neq i} \frac{q_j}{r_{ij}}\right) \quad (5)$$

where E_B^0 is free state binding energy, k is a constant which stands for the interaction between the inner electron shell and the valance electrons, q_i is the valance charge (negative) of atom i in a certain molecule, here refers to O, q_j is the valance charge (positive) of atoms, *i.e.* H here, bonded to atom i and r_{ij} is the average distance between the atom i and the atoms that bond to it. For H_2O molecules of different bound states, the chemical shift of peaks on XPS spectra can be described as the average contracting and prolonging O-H key length r_{ij}, allowing for other parameters are not changed for a given atom.

Table 2. Average O-H key lengths (Å) of H_2O molecules*.

	1	2	3	4
A	0.927^l	0.925^l	0.927^l	0.926^l
B	1.006^c	1.015^c	0.928^l	0.927^l
C	1.033^c	1.018^c	1.033^c	1.015^c

*A, B and C indicate the data from Figure 7d, Figure 7e and Figure 7f, respectively. The numbers from 1 to 4 correspond to the ones on H_2O molecules shown in Figure 7. The superscripts l and c stand for the data from l H_2O and c H_2O, respectively.

Table 3. Total interaction energy (a.u.) of SnO_2 lattice in Figure 7a-h.

a	**b**	**c**	**d**
28837.42	28840.54	28849.14	29247.01
e	**f**	**g**	**h**
28757.68	28402.20	28116.15	28116.15

As the data show, the average O-H key length of l H_2O is shorter than that of c H_2O and the total interaction energy is gradually diminished when l H_2O converses into c H_2O and finally evaporates leaving V_O as a result of annealing. Although the decreasing of total interaction energy well explains the increasing E_B value after 30 min annealing, the slight negative chemical shift of Sn3d and O1s peaks after 60 min annealing contradicts the calculation. Moreover, when l H_2O converts into c H_2O, the E_B value will decrease according to equation (5). Detailed calculation found that there is a ~0.1 eV drop of E_B, which is about half of the negative chemical shift of O2 peak, when the conversion completes. The conversion of coordinated water into free water will lead to the formation of extra V_O as well as the decreasing of O2/Sn which increases after 30 min annealing as Table 1 displays. Therefore, there must be another mechanism which determines the formation and annihilation of V_O.

Above analysis convinces that bound H_2O molecules cannot dominate the formation and annihilation of V_O and further the PL property of SnO_2 nanowire. Instead, the loosely bound O^{2-} ions in oxygen-defect regions are responsible for the O2 peak on XPS spectrum. In fact, 700 °C annealing temperature will create oxygen vacancies. Figure 7a-c are the illustrations of SnO_2 lattices. The 'bridging' oxygen atoms ($O_{Bridging}$) on the surface coordinate with their neighboring tin atoms, forming an angle of 100°. In vacuum, it has been observed that simple heating of a stoichiometric SnO_2 (1 1 0) surface to temperatures above 225 °C is liable to loss of $O_{Bridging}$ and formation of oxygen bridging vacancies [34,35] (Figure 8b). When the temperature is raised above 525 °C, the in-plane oxygen ($O_{In\ Plane}$) vacancies coordinating with neighboring Sn atoms forming an angle of 130° can be formed (Figure 8b) [34]. In our experiment, the two kinds of vacancy ought to exist for the synthesis temperature of about 800 °C and the annealing temperature of 700 °C at 10^{-3} Torr. Although the energetic O can compensate the vacancies when the product annealed in air, V_O inevitably forms. Considering the O compensation effect, after the products were annealed 30 min, the energetic O in air first occupy the surface V_O to form loosely bound O^{2-} ions leading to the increase of O2/Sn while more V_O are created in

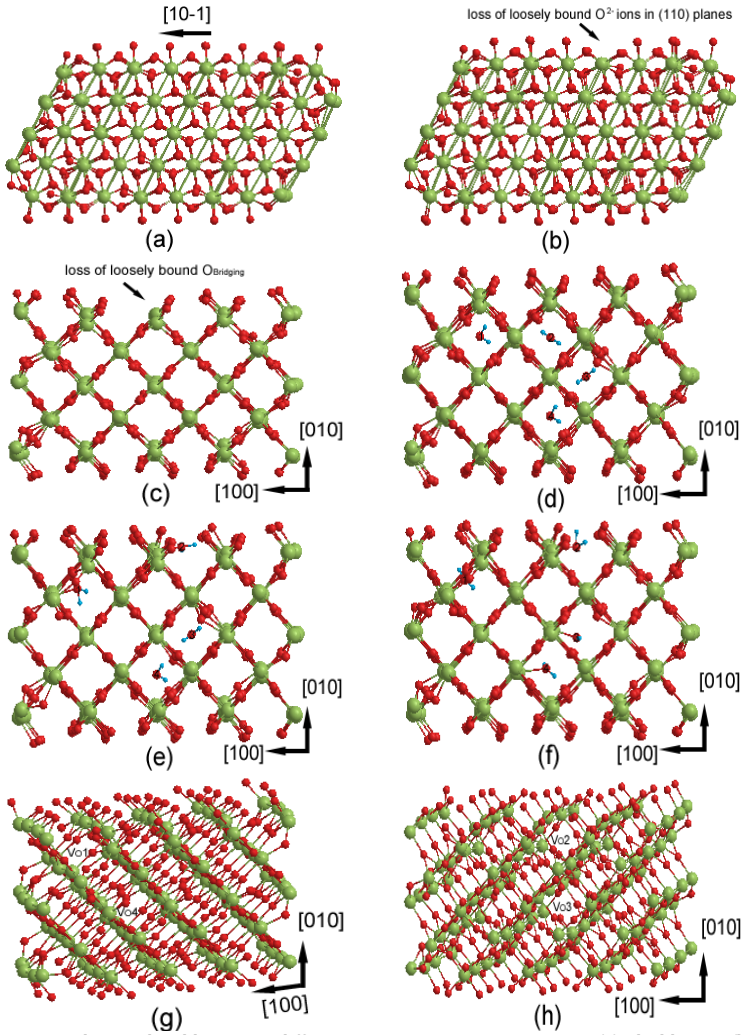

Figure 7. The simulated lattices at different steps in evaporation process: (a) ideal lattice, (b) lattice with loss of loosely bound O^{2-} ions in (110) planes, (c) lattice with loss of the 'bridging' oxygen, (d) four lattice H_2O molecules only, (e) coexisting lattice H_2O and coordinated H_2O, (f) four coordinated H_2O molecules only and (g) and (h) lattices of four oxygen vacancies after four coordinated H_2O evaporated. V_O1 and V_O2 are surface oxygen vacancies and V_O3 and V_O4 are the ones deep into the surface. The green balls stand for Sn atoms, the red ones for O atoms and the blue ones for H atoms, which is also the case for Figure 8.

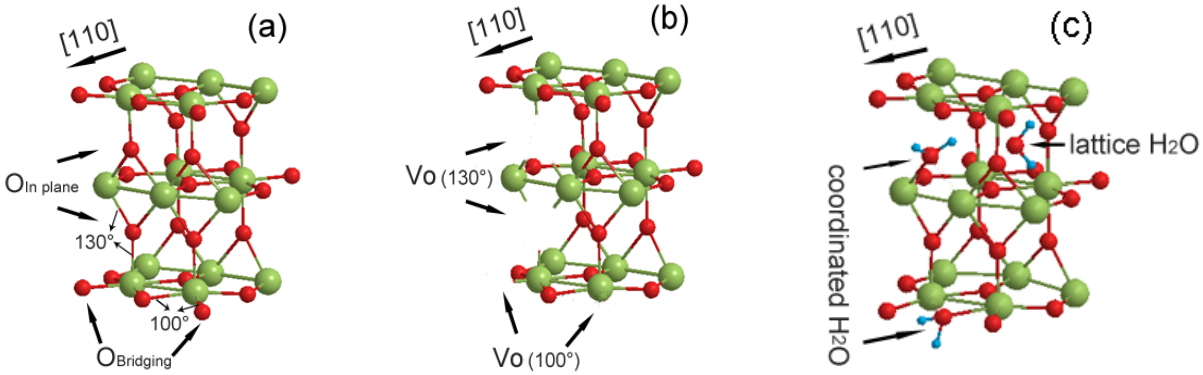

Figure 8. SnO_2 lattices with (a) two kinds of oxygen of $O_{Bridging}$ and $O_{In\ Plane}$, (b) the corresponding oxygen vacancy and (c) two kinds of bound H_2O molecules.

the lattice and the total interaction energy, displayed in Table 2, decreases, which explains the decreasing relative intensities of PL and positive chemical shift. Further 30 min annealing leads to the decrease of V_O in the surface region. Either the energetic desorbed loosely bound O^{2-} ions or the energetic oxygen in air will diffuse into the surface and cause the decrease of O2/Sn but increase of O1/Sn and negative chemical shift. The slight decrease of relative intensities of PL is due to the more additional V_O formation deep into the surface as long annealing time proceeds. The interaction between the shallow V_O and the deep V_O results in the level split created for the induction of the peak split as PL spectra shows. Figure 9 shows the illustration of the formation and annihilation of V_O.

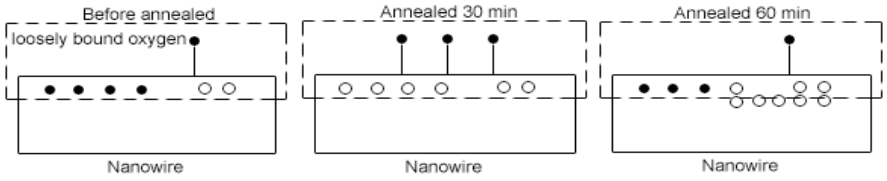

Figure 9. An illustration of the formation and annihilation of V_O. The black circle and the white circle depict the oxygen and V_O, respectively. The imaginary rectangle indicates the surface region.

4. Conclusion

SnO_2 cluster-system structures were synthesized via a two-step temperature-rising thermal evaporation method in short oxidation time of 25 minutes. While the 400 nm emission of the structures is attributed to the structural defects of nano-crystaline particles, the emissions at 453 nm, 459 nm is from the in-plane oxygen vacancies and the emission at 550 nm originates from the oxygen bridging vacancies. The increasing of V_O concentration as a result of annealing process leads to the diminishing of relative intensities of the newly found strong ultra-violet emissions while the green emission enhances, which is the combined action of the formation of V_O and the energetic O compensation. Our study provides a route to controlling the intensities of the violet emission and the green emission of SnO_2 cluster-system structures by simply annealing at 700 °C in air at 10^{-3} Torr. The violet emission and the strong green band emission can be obtained before and after annealing, respectively, which has potential application into excitation source in light-emitting diodes.

Acknowledgement

This work was financially supported by the National Natural Science Foundation of China (NSFC, No.20671027).

References

[1]. Li, F.; Chen, L. Y.; Chen, Z. Q.; Xu, J. Q.; Zhu, J. M.; Xin, X. Q. *Mater. Chem. Phys.* **2002**, *73,* 335-338.
[2]. Comini, E.; Faglia, G.; Sberveglieri, G.; Pan, Z. W.; Wang, Z. L. *Appl. Phys. Lett.* **2002**, *81,* 1869-1871.
[3]. Kolmakov, A.; Zhang, Y. X.; Cheng, G. S.; Moskovits, M. *Adv. Mater.* **2003**, *15,* 997-1000.
[4]. Arnold, M. S.; Avouris, P.; Pan, Z. W.; Wang, Z. L. *J. Phys. Chem. B* **2003**, *107,* 659-663.
[5]. Boyd, E. J.; Brown, S. A. *Nanotechnology* **2009**, *20,* 425201 (7 pp.).
[6]. Ferrere, S.; Zaban, A.; Gregg, B. A. *J. Phys. Chem. B* **1997**, *101,* 4490-4493.
[7]. Tatsuyama, C.; Ichimura, S. *Jpn. J. Appl. Phys.* **1976**, *15,* 843-847.
[8]. Seo, H. W.; Han, C. S.; Hwang, S. O.; Park, J. *Nanotechnology* **2006**, *17,* 3388-3393.
[9]. Luo, S.; Fan, J.; Liu, W.; Zhang, M.; Song, Z.; Lin, C.; Wu, X.; Chu, P. *Nanotechnology* **2006**, *17,* 1695-1699.
[10]. Tang, Y.; Zhao, D. X.; Shen, D. Z.; Zhang, J. Y.; Wang, X. H. *Nanotechnology* **2009**, *20,* 495601 (6 pp.).
[11]. Kim, T. W.; Lee, D. U.; Yoon, Y. S. *J. Appl. Phys.* **2000**, *88,* 3759-3761.
[12]. Sun, S. H.; Meng, G. W.; Zhang, G. X.; Gao, T.; Geng, B. Y.; Zhang, L. D.; Zuo, J. *Chem. Phys. Lett.* **2003**, *376,* 103-107.
[13]. Gu, F.; Wang, S. F.; Song, C. F.; Lu, M. K.; Qi, Y. X.; Zhou, G. J.; Xu, D.; Yuan, D. R. *Chem. Phys. Lett.* **2003**, *372,* 451-454.
[14]. Prades, J. D. *et al. Sensors and Actuators B* **2007**, *126,* 6-12.
[15]. Kim, T.W. *Mater. Res. Bull.* **2001**, *36,* 349-353.
[16]. Maestre, D.; Cremades, A.; Piqueras, J. *J. Appl. Phys.* **2004**, *95,* 3027-3030.
[17]. Ma, J.; Wang, Y. H.; Ji, T. F.; Yu, X. H.; Ma, H. L. *Mater. Lett.* **2005**, *59,* 2142-2145.
[18]. Gao, T.; Wang, T. H. *Mater. Res. Bull.* **2008**, *43,* 836-842.
[19]. Li, P. G.; Lei, M.; Tang, W. H.; Guo, X.; Wang, X. *J. Alloy. Compd.* **2009**, *477,* 515-518.
[20]. Mizokawa, Y.; Nakamura, S. *Jpn. J. Appl. Phys.* **1975**, *14,* 779-788.
[21]. Zhou, J. X.; Zhang, M. S.; Hong, J. M.; Yin, Z. *Solid State Commun.* **2006**, *138,* 242-246.
[22]. Wang, S. Solìd State Electronics, 1st edition, McGraw-Hill Book Co., 1966.
[23]. Jung, J.; Choi, S. P.; Chang, C. *Solid State Commun.* **2003**, *127,* 595-597.
[24]. Abello, L.; Bochu, B.; Gaskov, A.; Koudryavtseva, S.; Lucazeau, G.; Roumyantseva, M. *J. Solid State Chem.* **1998**, *135,* 78-85.
[25]. Zuo, J.; Xu, C.; Liu, X.; Wang, C.; Wang, C.; Hu, Y.; Qian, Y. *J. Appl. Phys.* **1994**, *75,* 1835-1836.
[26]. Diéguez, A.; Romano-Rodríguez, A.; Vilà, A.; Morante, J. R. *J. Appl. Phys.* **2001**, *90,* 1550-1557.
[27]. Liu, Y. K.; Zheng, C. L.; Wang, W. Z.; Yin, C. R.; Wang, G. H. *Adv. Mater.* **2001**, *13,* 1883-1887.
[28]. Mcguire, K.; Pan, Z. W.; Wang, Z. L.; Milkie, D.; Menéndez, J.; Rao, A. M. *J. Nanosci. Nanotech.* **2002**, *2,* 499-502.
[29]. Wang, J. X.; Lou, D. F.; Yan, X. Q.; Tuan, H. J.; Ci, L. J.; Zhou, Z. P.; Gao, Y.; Song, L.; Liu, L. F.; Zhou, W. Y.; Wang, G.; Xie, S. S. *Solid State Commun.* **2004**, *130,* 89-94.
[30]. Ye, J. D.; Gu, S. L.; Qin, F.; Zhu, S. M.; Liu, S. M.; Zhou, X.; Liu, W.; Hu, L. Q.; Zhang, R.; Shi, Y. *Appl. Phys. A* **2005**, *81,* 809-812.
[31]. Ogata, K.; Komuro, T.; Hama, K.; Koike, K.; Sasa, S.; Inoue, M.; Yano, M. *Phys. Status Solidi B* **2004**, *241,* 616-619.
[32]. Coppa, B.; Davis, R. F.; Nemanich, R. J. *Appl. Phys. Lett.* **2003**, *82,* 400-402.
[33]. Li, S.; Zhang, X. Z.; Yan, B.; Yu, T. *Nanotechnology* **2009**, *20,* 495604 (9 pp.).
[34]. Cox, D. F.; Fryberger, T. B.; Semancik, S. *Phys. Rev. B* **1988**, *38,* 2072-2083.
[35]. Cox, D. F.; Fryberger, T. B.; Semancik, S. *Surf. Sci.* **1990**, *227,* L105-L108.